Elucidating the Promotional Effect of Cerium in the Dry Reforming of Methane

Alberto Rodriguez-Gomez,*[a, b] Angeles Lopez-Martin,[a] Adrian Ramirez,[b] Jorge Gascon,[b] and Alfonso Caballero*[a]

A series of Ni-Ce catalysts supported on SBA-15 has been prepared by co-impregnation, extensively characterized and evaluated in the carbon dioxide reforming of methane (DRM). The characterization by TEM, XRD and TPR has allowed us to determine the effect of metal loading on metal dispersion. Cerium was found to improve nickel location inside the mesopores of SBA-15 and to suppress coke formation during the DRM reaction. The analysis by XPS allowed us to associate the high cerium dispersion with the presence of low-coordinated Ce^{3+} sites, being main responsible for its promotional effect. A combination of XAS and XPS has permitted us to determine the physicochemical properties of metals under reduction conditions. The low nickel coordination number determined by XAS in N-Ce doped systems after reduction suggests the generation of very small nickel particles which showed greater catalytic activity and stability in the reaction, and a remarkable resistance to coke formation.

Introduction

Cerium oxide has received considerable interest as a promoter for several catalytic applications including the selective oxidation of CO (PROX), water-gas-shift reaction (WGS), fluid catalytic cracking of petroleum (FCC), and as a component of the automotive three-way catalytic converters.[1–3] Most of the benefits of cerium promotion in heterogeneous catalysis are attributed to the Ce^{3+}/Ce^{4+} interconversion capacity which allows an enhanced oxygen mobility.[2–6] Moreover, the physical and chemical properties of the active metal phase could be modified in the presence of ceria, affecting the performance in hydrogen production reactions.[7–11] Hence, cerium oxide has been widely explored in the reforming of hydrocarbons, as a promoter of highly active noble metals (Pt, Rh)[7,12–15] or cheaper non-noble alternatives (Ni, Co).[16–21] Generally, cerium oxide (i) improves catalyst stability by preventing coke accumulation over the active metal surface, (ii) increases the catalytic activity by facilitating metal dispersion, and (iii) favors the activation of CO_2.

As mentioned before, the Ce^{3+}/Ce^{4+} redox couple is mainly responsible for the enhanced catalytic activity. However, understoichiometric CeO_{2-x} is mostly present in small nanoparticles with oxygen deficiency concentrated in low-coordinated cerium atoms on the surface.[22–25] This implies that, in a ceria supported system, the amount of Ce^{3+} is proportional to the dispersion of the oxide. However, the reducibility of ceria in a redox environment will also influence its chemical state. In this sense, many attempts were made to describe the promoter effect of cerium oxide in the catalytic dry reforming of methane (DRM).[12,16,20,26–30] Different characterization techniques have been utilized for that purpose, including temperature programmed reduction/oxidation (TPR/TPO), x-ray photoelectron spectroscopy (XPS) and x-ray absorption spectroscopy (XAS).[6,8,20,26,27,31] CeO_{2-x} goes through reduction/oxidation cycles along the reaction, enhancing oxygen mobility and coke gasification, thus improving the catalyst stability. Accordingly, an intimate contact between ceria and the active metal phase (coke promoter) should facilitate the process, and this can be addressed by using a high surface support.[32–34] On the other hand, a proper dispersion of the active metal phase has been shown to reduce graphitic coke formation by suppressing methane decomposition (the main source of coke at high temperatures),[35,36] a structure-sensitive reaction which is favored in larger crystal.[37,38] In this sense, several approaches has been explored to prevent metal aggregation as MgO-based solid-solution catalysts,[39–41] mixed metal oxide materials (as perovskites),[42,43] or co-impregnation with promoter oxides.[44–46]

Here, we studied five nickel-based systems promoted with cerium and supported in mesoporous silica SBA-15 for the DRM reaction. The catalysts were prepared by an ultrasonic-assisted incipient wetness impregnation method with different nickel loading and Ni/Ce atomic ratio. Both total metal loading and cerium content influence the metal dispersion and catalytic activity. By using in situ spectroscopies, we have (i) correlated the cerium dispersion with the availability of Ce^{3+} on surface (XPS), and (ii) determined the physicochemical state of nickel (XAS) under reaction conditions. A higher dispersion of both nickel and ceria increased the catalytic activity and selectivity in DRM reducing the level of coke formation. On the other hand,

[a] A. Rodriguez-Gomez, A. Lopez-Martin, Prof. A. Caballero
Instituto de Ciencia de Materiales de Sevilla (CSIC-University of Seville) and Departamento de Quimica Inorganica
University of Seville
41092 Seville (Spain)
E-mail: alberto.rodriguezgomez@kaust.edu.sa
caballero@us.es
[b] A. Rodriguez-Gomez, A. Ramirez, Prof. J. Gascon
KAUST Catalysis Center (KCC)
Advanced Catalytic Materials
King Abdullah University of Science and Technology
Thuwal 23955 (Saudi Arabia)

Supporting information for this article is available on the WWW under https://doi.org/10.1002/cctc.202001527

the temperature programmed reduction profiles show the effect of metal loading in the reducibility of ceria which is the key in its promoting effect.

Results and Discussion

Characterization of the calcined catalysts

The characteristic textural and structural properties of the SBA-15 support are illustrated in Figure S1. The N_2-adsorption/desorption isotherm of the calcined SBA-15 shows a hysteresis behavior at a relative pressure (p/p_0) higher than 0.45, associated to a Type IV (H1) ordered mesoporous material,[47] which is preserved after impregnation and calcination of the metal nitrate precursors (see Figure S1a). Pore size distribution shows a main pore width of 6.5–8 nm, the abundance of which decreases after metal loading. Moreover, the small-angle diffraction pattern (Figure S1b) shows an intense peak at 0.93° and two small ones at 1.64 and 1.89°, corresponding to the (100), (110) and (200) planes, respectively, associated to the two-dimensional hexagonal arrangement of SBA-15 which is clearly observed by TEM (Figure S1c).

The five xNiyCe/SBA-15 catalysts were submitted to characterization by N_2-adsorption analysis (BET, BJH), TEM, XRD, ICP, TPR, XPS and XAS. Some of the most characteristic physicochemical and textural properties of the catalysts are collected in Table 1. As shown, the specific surface area of the pristine SBA-15 decreased from 738 to 550–314 $m^2 g^{-1}$ after impregnation of both nickel and cerium nitrate precursors and subsequent calcination, being progressively lower at higher nickel-cerium content. Similarly, the pore volume decreased from 0.80 to 0.63–0.36 $cm^3 g^{-1}$. On the other hand, the TEM images in Figure 1 show that the structure of SBA-15 is preserved after impregnation and calcination of metal salts which give rise to the partial occupation of the mesoporous channels by the nickel-cerium phase that can be distinguish into dark aggregates. However, the distribution of the metallic phase depended on several factors: (i) the lower the nickel loading the better the metal dispersion, as can be seen in 5Ni- and 5Ni9Ce/SBA-15 samples (Figure 1a and 1b, respectively). Moreover, (ii) the addition of cerium clearly improved the homogeneity of the catalytic systems, especially in 5Ni9Ce/SBA-15 which shows most of the metallic phase inside the mesoporous structure, but also in 10Ni9Ce/SBA-15 compared to the analogous 10Ni/SBA-15 (Figure 1d and 1c, respectively) which shows a higher concentration of outer large aggregates. Finally, (iii) an excess of cerium loading resulted in the aggregation of the metallic phase as shown in the image corresponding to the 10Ni18Ce/SBA-15 sample (Figure 1e).

The x-ray diffraction diagrams in Figure 2a display the formation of a NiO cubic phase in all the calcined catalysts as well as peaks associated with the fluorite-type structure of CeO_2 in cerium doped systems. Interestingly, the NiO crystallite size estimated by the Scherrer equation decreased from 19 nm, in both monometallic systems, to a not-determined value in 5Ni9Ce/SBA-15 due to peaks width which indicates the generation of very small crystals, and to 15 nm in 10Ni9Ce/SBA-15. Besides, the average crystallite size of NiO at high cerium loading increased to 37 nm. On the other hand, the CeO_2 average crystallite sizes of 3, 4 and 6 nm in 5Ni9Ce-, 10Ni9Ce- and 10Ni18Ce/SBA-15, respectively, indicates a high dispersion of the ceria phase in the three bimetallic Ni-Ce catalysts.

The reducibility of the calcined systems has been followed by temperature programmed reduction (TPR) measurements. According to the profiles shown in Figure 3a, the monometallic systems present two main reduction processes with peaks centered at 340–370 and ca. 520 °C. The first peak appears at the same temperature range of bulk NiO while the second one can be ascribed to NiO in a stronger interaction with the support, as expected for NiO clusters inside the channels of SBA-15.[48] In most of the samples, the peak assigned to bulk NiO shows at least two components at ca. 314 and 365 °C which would indicate different grades of NiO aggregation in surface of the support. This correlates with the highest prominence of the peak at lower temperature and the almost negligible component at ca. 500 °C in 10Ni18Ce/SBA-15 which shows a greater aggregation of the metallic phase (see Figure 1e, TEM). Moreover, the peaks at 314 and 365 °C have been shifted to 340 and 388 °C, respectively, in both 5Ni9Ce- and 10Ni9Ce/SBA-15 which can be ascribed to a more effective NiO-CeO_2 interaction. On the other hand, the reducibility of ceria must be taken into account for a complete interpretation of the TPR profiles. The reduction of massive ceria is expected at temperatures above 750 °C while several authors have described the reduction of surface CeO_x species at low temperature (< 500 °C), in the same range of NiO.[49–51] The H_2 consumption in the partial reduction of ceria could be estimated by assuming the total trans-

Table 1. Specific surface areas and pore volume obtained from N_2 adsorption/desorption isotherms. Ni and Ce weight percentage measured by ICP, average crystallite size by the Scherrer Equation, elemental atomic percentages calculated from XPS Spectra, and H_2 consumption from a TPR experiment of the xNiyCe- supported in SBA-15 systems.

Catalyst calcined at 550 °C	S_{BET} [$m^2 \cdot g^{-1}$]	V_T [$cm^3 \cdot g^{-1}$][a]	ICP [wt.%]		Scherrer Ø [nm]		$[X^{n+}]_{surface}$ [at.%][b]				H_2 consumption [$mmol \cdot g^{-1}$]	
			Ni	Ce	NiO	CeO_2	Ni	Ce	Si	O	Total	CeO_x[c]
SBA-15	738	0.80	–	–	–	–	–	–	32.5	63.6	–	
5Ni-	550	0.63	4.8	–	19	–	1.1	–	32.8	64.6	0.84	–
10Ni-	439	0.56	10.3	–	19	–	1.9	–	32.3	64.0	1.71	–
5Ni9Ce-	421	0.52	5.0	9.4	n.d.	3	0.9	0.8	31.7	64.9	1.47	0.62
10Ni9Ce-	377	0.46	9.9	9.2	15	4	2.1	1.2	30.7	62.5	2.20	0.50
10Ni18Ce-	314	0.36	9.5	19.0	37	6	2.3	1.0	30.9	63.5	2.13	0.43

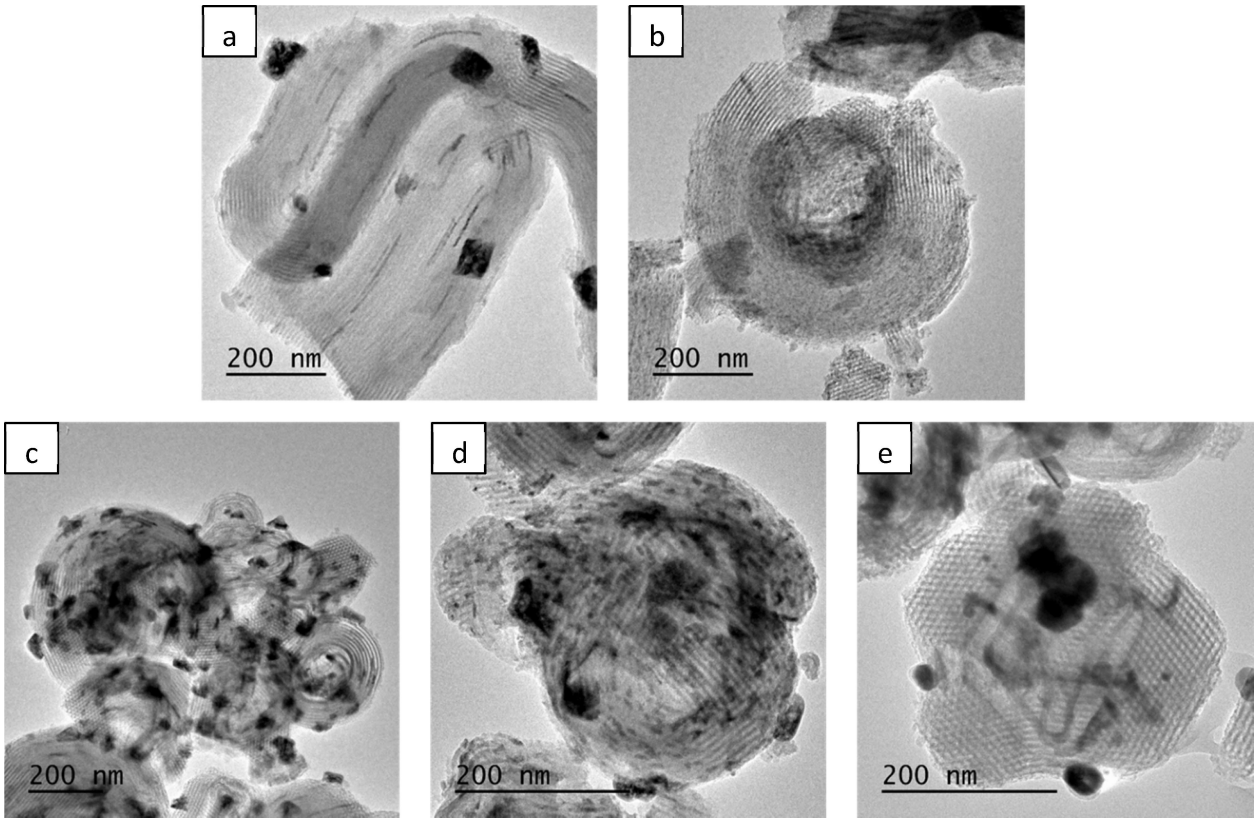

Figure 1. TEM images of as-made 5Ni- (a), 5Ni9Ce- (b), 10Ni- (c), 10Ni9Ce- (d) and 10Ni18Ce/SBA-15 (e).

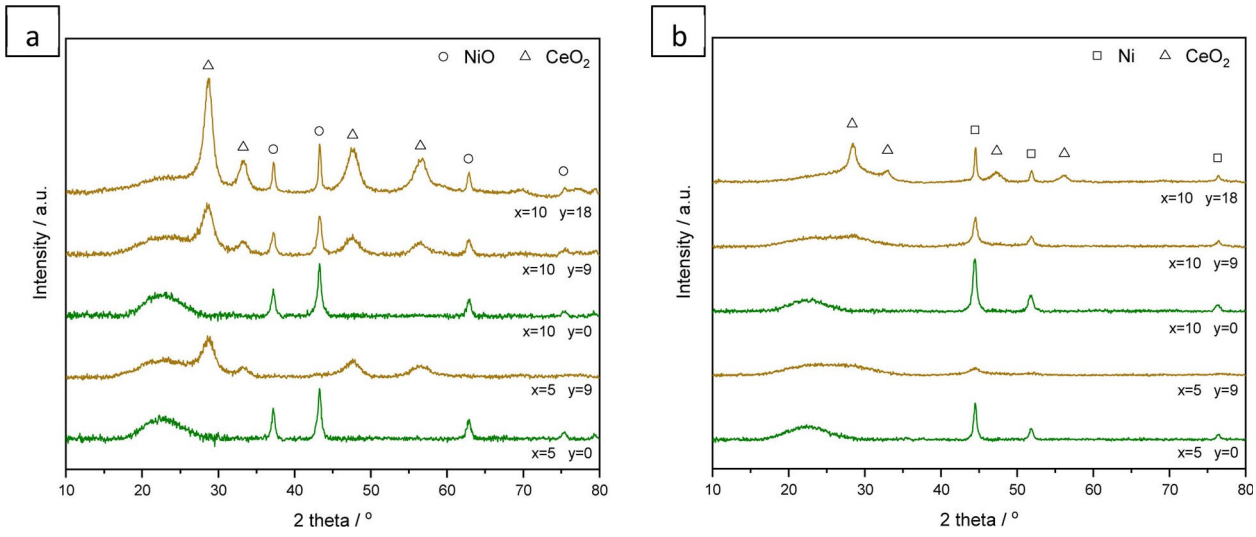

Figure 2. Powder x-ray diffractograms of the as-made (a) and reduced in a 5% H_2/Ar gas mixture at 750 °C (b) xNiyCe/SBA-15 systems.

formation of NiO into metallic nickel along the TPR experiment. As shown in Table 1, a consumption of 0.62, 0.50 and 0.43 mmol g^{-1} of H_2 is found for 5Ni9-, 10Ni9Ce- and 10Ni18Ce/SBA-15, respectively. According to the following reaction: $2CeO_2 + H_2 \rightarrow Ce_2O_3 + H_2O$, these values represent a reduction of 97, 78 and 33% of the total CeO_2 phase in each case.

Figure 3b displays the CO_2-TPD profiles of the xNiyCe/SBA-15 catalysts which accounts for the basicity of the samples. The presence of basic sites on the catalyst surface leads to a greater adsorption and activation of carbon dioxide which can react with CH_x species but also with the carbon deposited on surface by the reverse Boudouard reaction ($C + CO_2 \rightarrow 2CO$). As seen, both monometallic catalysts show a negligible adsorption of

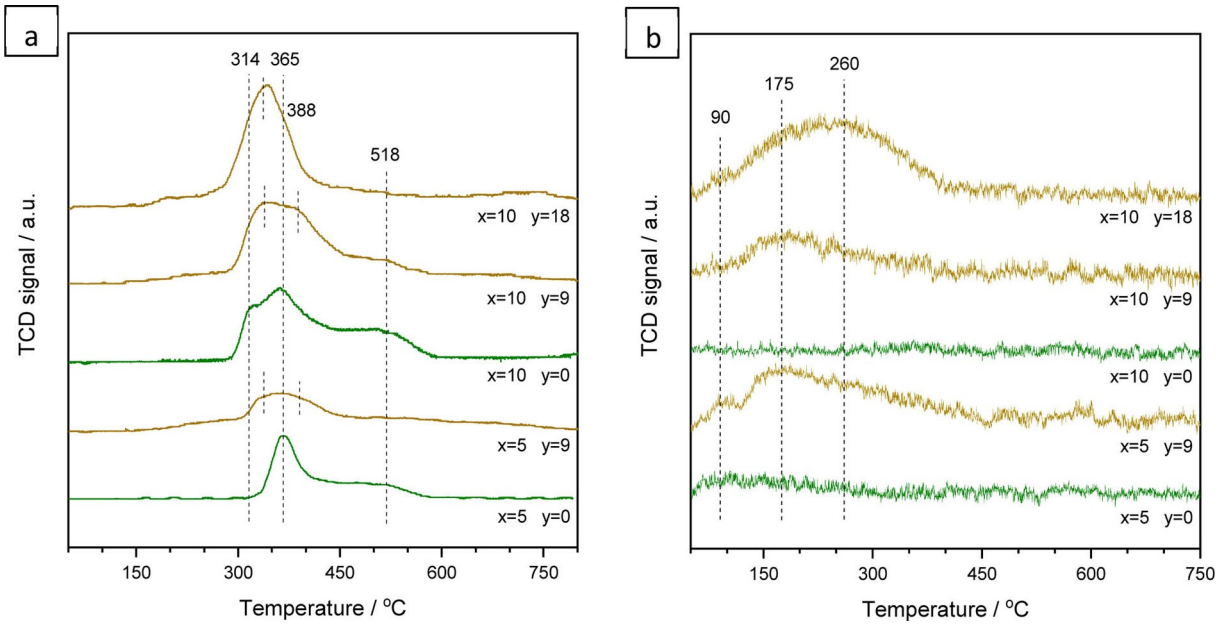

Figure 3. Temperature-programmed reduction profiles of the as-made xNiyCe/SBA-15 systems (a) and temperature-programmed desorption of CO_2 profiles of the pre-reduced catalysts (b).

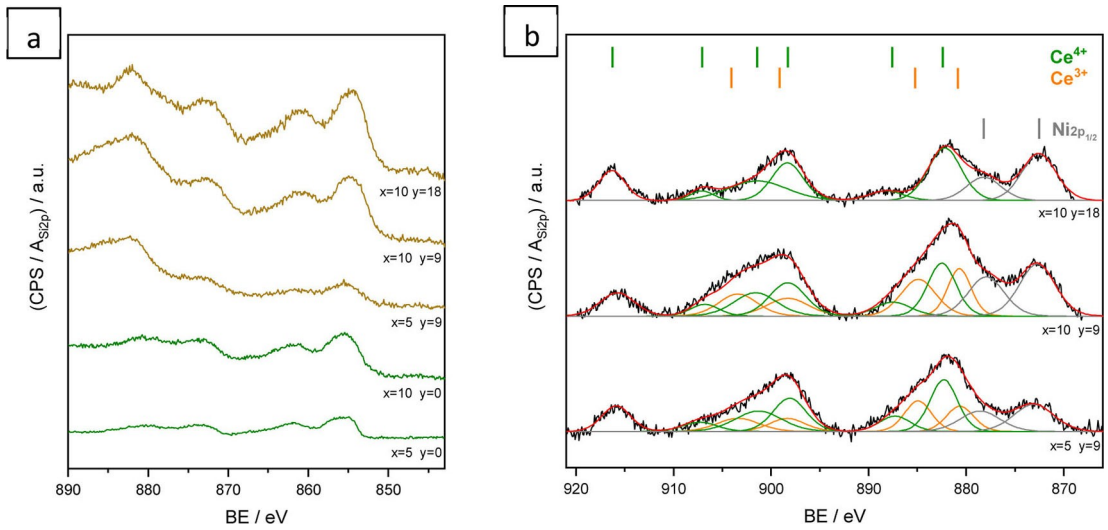

Figure 4. XPS spectra of the as-made xNiyCe/SBA-15 systems in the Ni 2p (a) and Ce 3d (b) regions. Ce^{4+}, Ce^{3+} and Ni $2p_{1/2}$ contributions are colored in green, orange and gray, respectively. Red line represents the fitted peaks envelope.

carbon dioxide while the incorporation of ceria allows for better capacity, as the peaks in the 50–450 °C range show. Generally, the desorption of carbon dioxide at temperatures below 200 °C can be ascribed to a weak basicity, this being the case of the 5Ni9Ce- and 10Ni9Ce/SBA-15 samples which show a main peak at 175 °C and a secondary one at 90 °C. In addition to the peaks at low temperature, the 10Ni18Ce/SBA-15 exhibits a main peak at 260 °C with a wide shoulder up to 450 °C associated to the decomposition of carbonate species in moderate basic sites[52] which is also present in 5Ni9Ce/SBA-15. Taking into account the relative intensity of the peaks and total adsorption of CO_2, the order in basicity can be stablished as 10Ni18Ce- (17.6 $\mu mol\,g^{-1}$) > 5Ni9Ce− (16.0 $\mu mol\,g^{-1}$) > 10Ni9Ce− (7.9 $\mu mol\,g^{-1}$) ≫ 5Ni- ≈ 10Ni/SBA-15 (> 1 $\mu mol\,g^{-1}$).

Next, the physicochemical state of the calcined Ni-Ce bimetallic catalysts was analyzed by XPS. Figure 4 plots the recorded signals of Ce3d and Ni2p regions. Despite the coupling between the Ce3d$_{5/2}$ and Ni2p$_{1/2}$ signals, the well resolved Ni2p$_{3/2}$ peak with maximum at ca. 855 eV can be assigned to Ni^{2+} (Figure 4a). Meanwhile, the analysis of the Ce3d signal is rather complex due to (i) the coupling between 5/2 and 3/2 spin-orbit split components, (ii) the co-existence of

both Ce^{3+} and Ce^{4+} associated electronic configurations, and (iii) the $Ni2p_{1/2}$ interference at lower binding energy. With the aim of estimating the $Ce^{3+}/(Ce^{3+}+Ce^{4+})$ atomic ratio on catalyst surface, the Ce3d signal envelope was constructed using a Shirley background and symmetric Gaussian-Lorentzian functions for each component. The analysis was done using the nomenclature given by Burroughs et al.[53] (see Figure 4b), commonly applied by other authors in cerium based systems.[54–57] Accordingly, the $Ce^{3+}/(Ce^{3+}+Ce^{4+})$ ratio is given by the following equation [Eq. (1)]:

$$\frac{Ce^{3+}}{Ce^{3+}+Ce^{4+}} = \frac{v^0+v'+u^0+u'}{v^0+v'+u^0+u'+v+v''+v'''+u+u''+u'''} \quad (1)$$

This way, values of 0.33, 0.43 and 0 were estimated for the 5Ni9Ce-, 10Ni9Ce- and 10Ni18Ce/SBA-15 catalysts, respectively. According to the given ratios, both 5Ni9Ce- and 10Ni9Ce/SBA-15 catalysts present a high concentration of Ce^{3+} on surface which has been directly associated to the availability of low-coordinated cerium atoms on edge sites, as expected in very small ceria nanoparticles.[58] A higher concentration of these sites has been found to enhance the catalytic activity in redox reactions.[59]

Finally, the calcined systems were also analyzed by XAS in the Ni K-edge region. As shown in Figure 5a, all the samples present the typical XANES features of a cubic NiO reference with the maximum being the white line at 8350 eV. On the other hand, Fourier Transforms of the EXAFS region included in Figure 5b (with phase correction) display two main peaks at low radial distances corresponding to Ni–O_1 (1.9 Å) and Ni-Ni_2 (2.8 Å), first and second coordination sphere, respectively. A decrease of the Ni-Ni_2 amplitude could indicate a distortion of the NiO lattice thus annulling the strong multiple scattering effect for paths involving collinear atoms in the cubic phase.[60,61] This is found in the 5Ni9Ce/SBA-15 sample, either owing to the small NiO crystallite size or to the incorporation of cerium in the structure.

In situ XPS and XAS study under reduction conditions

The Ni-Ce systems have been studied in situ by XPS and XAS under reduction conditions. The spectra were collected using a 5% H_2/Ar flow from room temperature (RT) up to 750 °C, mimicking the pre-treatment conditions before catalytic test (vide supra). Figure 6 shows the high-resolution spectra of the Ce3d and Ni2p regions after the treatment in a 5% H_2/Ar mixture at 750 °C. At these conditions, nickel has been totally reduced to Ni^0 with a maximum of the $Ni2p_{3/2}$ signal at 851.7 eV (Figure 6a). Moreover, most of the cerium presents a+3 oxidation state in the three Ni–Ce bimetallic catalysts (Figure 6b) while the components associated to Ce^{4+} are only relatively intense in the 10Ni18Ce/SBA-15 sample, representing ca. 15% of the total cerium on surface (see Table 2). Similarly, the XRD pattern of the reduced samples included in Figure 2b show peaks associated to metallic nickel in all the cases while the peaks associated to CeO_2 are almost negligible, except in the 10Ni18Ce/SBA-15 sample. Interestingly, the intensity of both Ni2p and Ce3d spectra increases at higher total metal loading in analogous systems (i.e., 10**Ni**18Ce > 10**Ni**(9Ce), and 10Ni9**Ce** > 5Ni9**Ce**, respectively) while both XRD and TEM (Figure S2) results indicate the opposite, i.e. the higher the Ni-Ce loading the lower the metal dispersion. This has already been explained by our group as an effect of metal location inside the mesopores of SBA-15 which make it invisible to XPS.[48] As shown by TEM images of the reduced samples (Figure S2), most of the bimetallic nanoparticles obtained after reduction of 5Ni9Ce/SBA-15 are aligned with the well-defined channels of the support. Figure 7 shows the in situ XAS analysis of the catalysts submitted to hydrogen treatment at 500 and 750 °C. The XANES spectra of the catalysts after treatment at 500 °C (Figure 7a) show similar features to a nickel foil reference

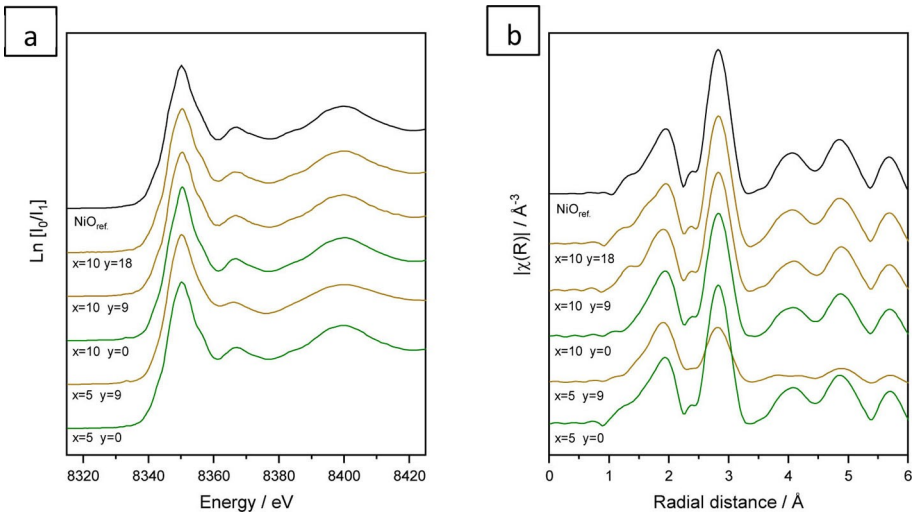

Figure 5. Ni–K edge XANES spectra (a) and Fourier transform functions of the EXAFS oscillations (b) of the calcined xNiyCe/SBA-15 systems.

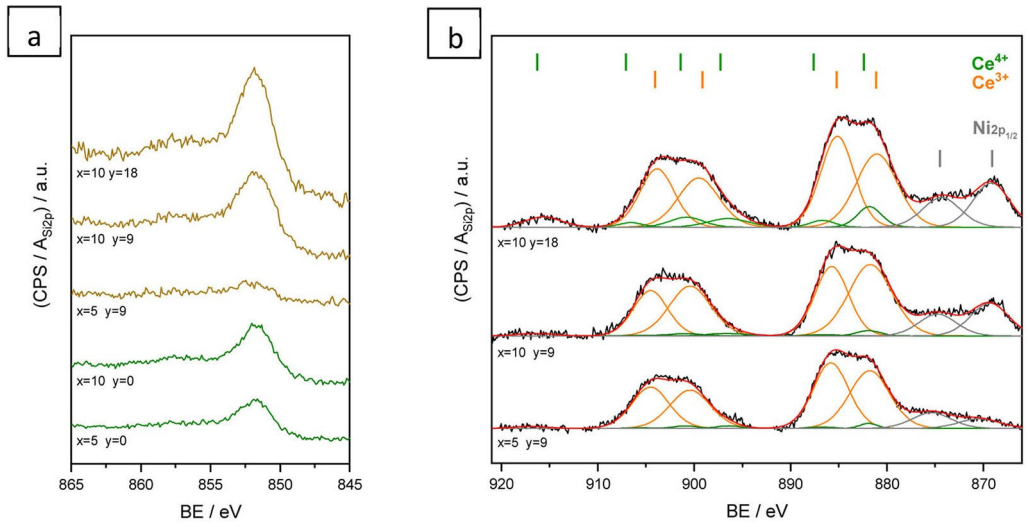

Figure 6. XPS spectra of the reduced xNiyCe/SBA-15 systems in the Ni 2p (a) and Ce 3d (b) regions. Ce^{4+}, Ce^{3+} and Ni $2p_{1/2}$ components are colored in green, orange and gray, respectively. Red line represents the fitted peaks envelope.

Table 2. [a] V_T symbol corresponds to the single point pore volume at p/p $_0$ = 0.965 of the nitrogen adsorption isotherm. [b] Calculated from the XPS spectra. [c] Calculation based on the total reduction of nickel.Table 2
Ce^{3+} concentration on surface estimated from the fitting of the Ce 3d XPS signal, nickel oxide percentage calculated from the Ni–K edge XANES spectra, best-fitting values obtained from the FT of the Ni–K edge EXAFS spectra of the catalysts reduced at 750 °C and average particle size estimated by TEM.

Catalyst	Ce^{3+} / (Ce^{3+} + Ce^{4+}) [a]		NiO % [b]		Best-fit values from EXAFS of reduced samples [c]				Average Ni particle size [nm][d]
	Calcined	H_2, 750 °C	H_2, 500 °C	H_2, 750 °C	CN	ΔE^0	R	D–W (Å^2 x 10^{-3})	
5Ni-	–	–	22	0	11.0	7.0	2.48	6.5	10.9
10Ni-	–	–	12	0	11.2	7.0	2.48	6.5	11.1
5Ni9Ce-	33	98	29	0	10.1	6.7	2.48	7.0	2.6
10Ni9Ce-	43	97	15	0	10.8	6.8	2.48	5.9	6.1
10Ni18Ce-	0	85	6	0	11.8	6.7	2.48	5.9	14.6

[a] Estimated from the Ce 3d XPS signal analysis. [b] Calculated by linear combination of XANES spectra. [c] Measured at RT after reduction and referred to CN = 12 and R = 2.48 Å of a reference Ni foil. [d] Calculated from the TEM histograms of reduced samples (Figure S2).

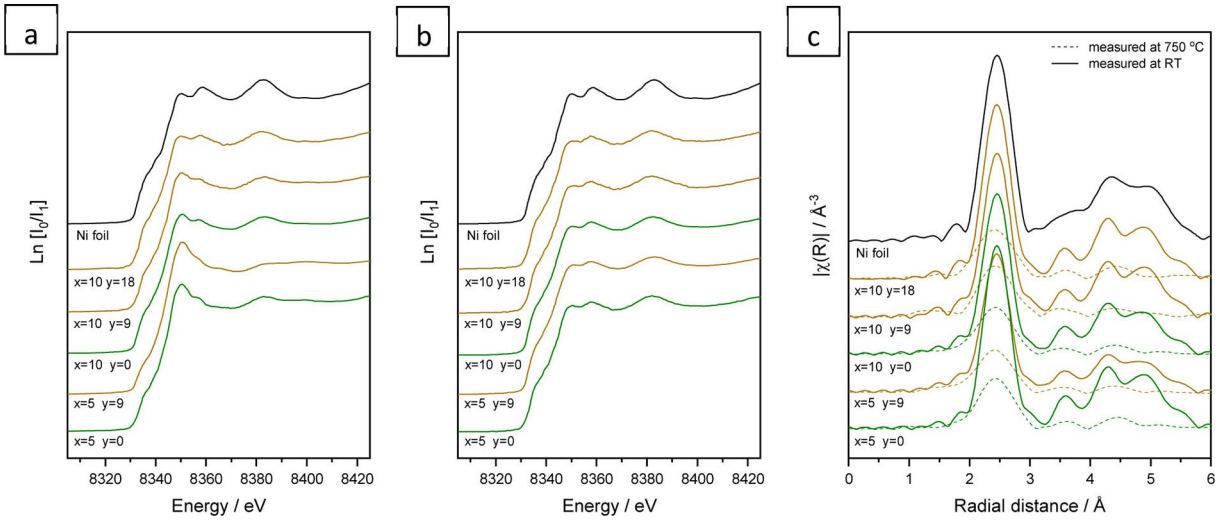

Figure 7. Ni–K edge XANES spectra of the reduced xNiyCe/SBA-15 catalysts at 500 (a) and 750 °C (b), and Fourier transform functions of the EXAFS oscillations (c) after reduction at 750 °C.

but with some changes in the white line (8349 eV), particularly in its relative intensity, which indicates the dominance of nickel oxide. A lineal combination fitting of the spectra shows the remanence of Ni^{2+} in a 22, 29, 12, 14 and 6% for 5Ni-, 5Ni9Ce-, 10Ni-, 10Ni9Ce- and 10Ni18Ce/SBA-15, respectively, i.e. it increases in the same way as nickel dispersion. Next, the treatment at 750 °C gives rise the complete reduction of nickel in all the samples, as can be seen in both XANES and FT of EXAFS spectra displayed in Figure 7b–c, showing a maximum in amplitude of the first coordination sphere at 2.46 Å (Ni–Ni_1). The analysis of the radial distribution pseudo-function, based on FEFF calculations from a metallic nickel reference (fcc), provides information about the Ni-Ni_1 coordination number (CN) which can be correlated with the nickel particle size since the contribution of low-coordinated surface atoms in nanoparticles gives rise to an average CN appreciably lower than 12 (bulk nickel).[62] Taking into account the temperature dependence of the Debye-Waller factor, the fitting analysis were done over the recorded spectra at room temperature (Figure 7c) while CN was estimated from the Ni-Ni_1 amplitude of a Ni foil reference (CN = 12). This way, it has been estimated a CN of 11.0, 10.1, 11.2, 10.8, 11.8 for 5Ni-, 5Ni9Ce-, 10Ni-, 10Ni9Ce- and 10Ni18Ce/SBA-15, respectively. In a model of pseudo-spherical particles, a CN in the 10–10.5 range would correspond to average particle sizes of 2–4 nm while CN > 11.5 is associated to particle sizes above 10 nm.[63,64] The details of the fitting parameters for both XANES and EXAFS regions are recorded in Table 2.

As an initial summary, it can be rated that both the lower metal loading and cerium doping improved the nickel dispersion as shown by TEM (Figure 1) and XRD (Figure 2). This resulted in a lower reducibility of the nickel oxide phase and the formation of smaller nickel particles after total reduction at 750 °C, as indicated the analysis of the average coordination number by XAS. CO_2-TPD experiments has proven the role of ceria in the greater CO_2 adsorption capacity, especially at the highest cerium loading. On the other hand, it has been observed that both the dispersion and reducibility of ceria improve at lower Ni-Ce content. A consequence of this high dispersion is the presence of low-coordinated Ce^{3+} species on surface in both 5Ni9Ce- and 10Ni9Ce calcined systems (Figure 4b) which presumably is key in its promotional effect under reaction conditions. This will be examined with the catalytic results.

Catalytic studies

The five catalysts were evaluated at 750 °C using a 1/1/1 CH_4:CO_2:N_2 gas mixture at atmospheric pressure, where the equilibrium conversion of CH_4 and CO_2 is ca. 90 and 95%, respectively.[65,66] Thus, the residence time effect was previously evaluated to work below thermodynamic control. As shown in Figure 8, the activity differs drastically between monometallic and cerium-doped systems. Initially, the conversion of methane (Figure 8a) reaches 80% in both 5Ni9Ce- and 10Ni9Ce/SBA-15, 70% for 10Ni18Ce/SBA-15 catalyst, while it barely reaches 50%

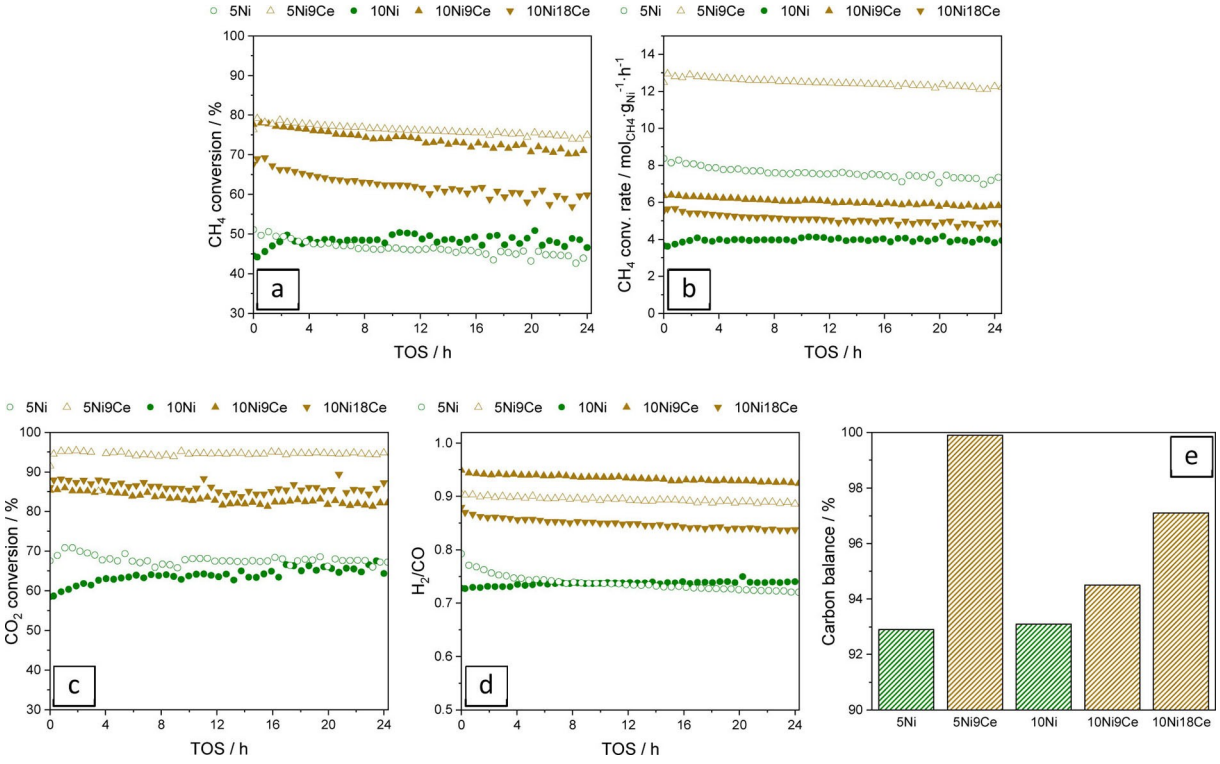

Figure 8. CH_4 conversion (a) and reaction rate (b), CO_2 conversion (c), H_2/CO ratio (d) and average carbon balance in gas phase (e) of the xNiyCe/SBA-15 catalysts in the DRM reaction at 750 °C and WHSV = 60000 mL min^{-1} gcat^{-1} for 24 hours.

in both monometallic catalysts. These results can be expressed as a function of nickel loading which underlines that methane reaction rate (mol $CH_4 \cdot g^{-1}$ Ni per hour, Figure 8b) is improved at lower metal loading with values of 8 and 13 $mol \cdot gNi^{-1} \cdot h^{-1}$ in both 5Ni- and 5Ni9Ce/SBA-15, respectively, doubling the measured values of the analogous 10Ni- and 10Ni9Ce-SBA-15. On the other hand, the effect of cerium is also reflected in a higher reaction rate. The greater activity seems to correlate in both cases to the better nickel dispersion.

The stability was examined throughout the 24 hours of reaction. The more active bimetallic 5Ni9Ce-, 10Ni9Ce- and 10Ni18Ce/SBA-15 catalysts displayed a decrease of 6, 11 and 15% in methane conversion, respectively. The lower deactivation rate in the 5Ni- and 10Ni/SBA-15 catalysts can be ascribed to their lower activity. On the other hand, the H_2/CO ratio (Figure 8d) was clearly improved by cerium, with values of ca. 0.9, 0.95 and 0.85 in the bimetallic 5Ni9Ce-, 10Ni9Ce- and 10Ni18Ce/SBA-15 samples, respectively, being lower than 0.75 in both monometallic systems indicating a high reverse water-gas shift activity ($CO_2 + H_2 \rightarrow CO + H_2O$). Moreover, the carbon balance in gas phase (Figure 8e) is closed above 90% in all the cases but clearly improved at higher Ce/Ni ratio, achieving a 99.9% in the 5Ni9Ce/SBA-15 catalyst. The latter shows a higher CO_2 conversion (Figure 8c) compared with the analogous 10Ni9Ce/SBA-15 sample (95 and 85%, respectively), presumably toward CO thus lowering the H_2/CO ratio. Therefore, it can be stablished that ceria improves the carbon balance by preventing coke formation nevertheless a high Ce/Ni ratio can be detrimental by improving CO_2 activation toward secondary reactions (as RWGS). Despite the above, the effect of particle size in coke formation should not be neglected since it has been seen that only large nickel particles, generally bigger than 5–7 nm, are responsible for the formation of filamentous carbon.[67–69]

Additionally, the XPS C 1s signal of the samples submitted to the in situ DRM reaction (see Figure S3) shows two main components at 284.6 and ca. 281 eV, typically associated with C–C species and metal carbide, respectively. The first dominates in both 10Ni- and 10Ni18Ce/SBA-15 catalysts while the carbide contribution is only visible in the cerium-doped systems, relatively intense in the 10Ni9Ce/SBA-15 and almost negligible in both 5Ni9Ce- and 10Ni18Ce/SBA-15 catalysts. In line with this, the XRD patterns of the spent samples (Figure S4) show intense peaks associated with graphite in the monometallic 10Ni/SBA-15 catalyst which decrease at higher Ce/Ni ratio. It could be hypothesized that cerium prevents the formation of C–C bonds which occurs by a metal carbide intermediate (see Scheme 1). In fact, this mechanism has been already proposed for the methane decomposition reaction,[70–72] main source of coke at these reaction conditions, which is favored in larger nickel aggregates (as in the case of 10Ni- and 10Ni18Ce/SBA-15 samples).[37,38]

Conclusions

In summary, we have characterized a series of nickel-based catalysts promoted with ceria prepared by incipient wetness co-impregnation of SBA-15. Altogether, our results demonstrate that: (i) both lower metal loading and co-impregnation of cerium improved metal dispersion inside the mesoporous structure of SBA-15; (ii) the nickel resistance to reduction is improved at higher metal dispersion giving rise to smaller particles after a 5% H_2/Ar treatment at 750 °C. Conversely, ceria reducibility was improved; (iii) the promotional effect of ceria was clearly demonstrated during the catalytic tests by improving the H_2/CO ratio and carbon balance. On the other hand, the enhanced CO_2 activation by ceria (CO_2-TPD) can also promote

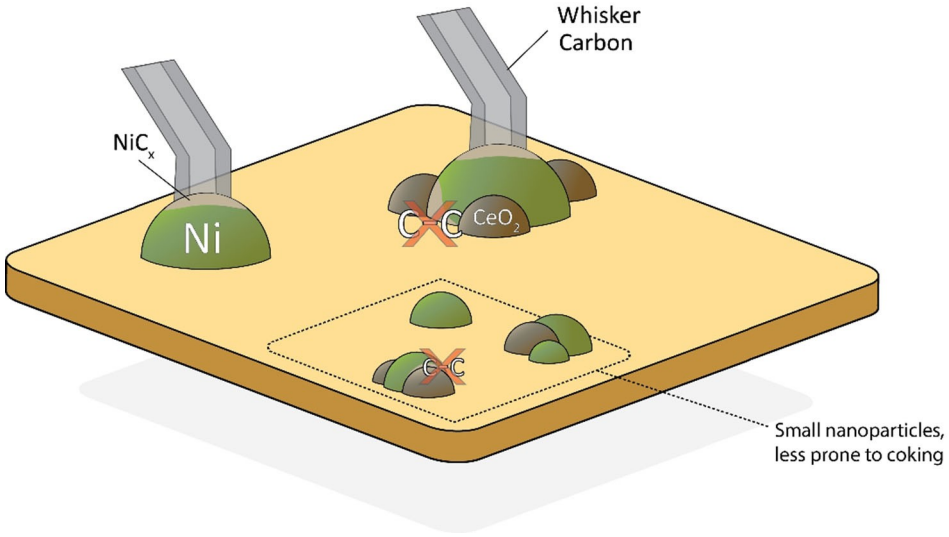

Scheme 1. Proposed mechanism for coke suppression by ceria during the DRM reaction. The structure-sensitive methane decomposition reaction over nickel gives rise to the formation of whisker carbon which grows from a NiC_x intermediate. Ceria nanoparticles in direct contact with carbide species prevents C–C propagation through the CO_2 activation.

undesirable secondary reaction as RWGS. Therefore, the Ce/Ni has to be properly adjusted.

Finally, in view of the catalytic results and the in situ C 1s XPS analysis of the spent catalysts we proposed a reaction mechanism where ceria avoids coke formation by suppressing the propagation of C–C bonds chain from a nickel carbide intermediate, precursor of filamentous carbon over metallic nickel surfaces.

Experimental Section

Catalysts preparation. SBA-15 mesoporous silica support was prepared according to the protocol reported by our group,[48] based in Zhao's novel work published in 1998.[73] Typically, 3 g of P123 (Sigma-Aldrich, CAS: 9003-11-6) was dissolved in 140 mL of hydrochloric acid 1.8 M and heated up to 45 °C. Then, 5.9 mL of tetraethyl orthosilicate (Sigma-Aldrich, CAS: 78-10-4) was added to the solution revealing the formation of a white dispersion. After an aging period of 18 h at 45 °C, the resulted white product was filtered in a Büchner funnel, washed with enough boiling water to completely remove the surfactant, dried at 150 °C and calcined for 3 h at the temperature of 550 °C using a ramp of 1 °C·min^{-1}. The nickel and cerium metal phases were loaded on 1 g of as-made SBA-15 by an ultrasonic-assisted incipient wetness impregnation method using $Ni(NO_3)_2 \cdot 6H_2O$ (Panreac, CAS: 13478-00-7) and $Ce(NO_3)_3 \cdot 6H_2O$ (Sigma-Aldrich, CAS: 10294-41-4) as precursors. After that, the powder was dried at 120 °C for 24 h and calcined at the temperature of 550 °C. The resulting catalysts were labelled as xNiyCe/SBA-15, where x and y represent the wt. % of nickel (x = 5 or 10) and cerium (y = 0, 9 or 18).

N_2 physisorption. Nitrogen adsorption/desorption isotherms were obtained on a TriStar II (Micromeritics) instrument at the temperature of 77 K. Catalysts were dried under vacuum at 170 °C for 12 h prior to the measurements. Specific surface area and pore size distribution were estimated in the relative pressure range of 0.05–0.25 according to the BET and BJH methods,[74,75] respectively. Total pore volume was obtained from a single point measurement at $P/P_0 = 0.965$.

ICP. Inductively coupled plasma analysis for Ni and Ce was carried out using a 5100 ICP-OES instrument and SPS 4 Autosampler (Agilent), using argon as gas supply. Prior digestion of the samples, vessel was cleaned in nitric acid (5 mL). Two different digestion protocols were used: (1) a solution containing aqua regia and HF for nickel analysis, and (2) a solution of concentrated HCl for cerium analysis; at max 30 bar and 240 °C bar in an UltraWAVE equipment (Milestone), in both cases. A calibration curve (4 plots) was built (1-10-25-100 ppm) and all samples have been duplicated.

PXRD. Powder x-ray diffractograms has been measured in a PANalytical X-Pert PRO instrument using a Cu Kα source (λ = 1.5418 Å) in a Bragg – Brentano geometry, equipped with an X'Celerator and a RTMS x-ray detector (active range of 2θ = 2.18°). Data were acquired in the 2θ range of 10–80°, a step of 0.05°, and 250 s of acquisition time. The analysis of diffractograms was carried out using the X'Pert HighScore Plus v4.0 software (PANalytical).

TPR. Temperature programmed reduction profiles were measured using a TCD detector and commercial CuO (Sigma-Aldrich) for intensity calibration. A sample amount selected for consumption of ca. 100 μmol-H_2 was pre-treated in argon at 110 °C, cooled down up to 35 °C and submitted to a reduction treatment in 50 mL min^{-1} of 5% H_2/Ar (calibration mix) until 800 °C using a heating ramp of 10 °C min^{-1}. All experimental parameters were carefully adjusted to prevent peak coalescence.[76]

CO_2-TPD. Temperature programmed desorption of carbon dioxide experiments were conducted in an AMI-200 Altamira equipment. Before the experiment, circa 80 mg of pelletized sample (150–250 μm) were placed in a U shaped quartz reactor and pre-reduced in 5% H_2/Ar flow at 750 °C. After cooling to 35 °C, a mixture of 25% CO_2/He was passed through the reactor for 30 minutes. Then, the sample was flashed with 30 mL min^{-1} of helium flow for 15 minutes to purge the non-adsorbed carbon dioxide and heated up to 750 °C with a heating ramp of 10 °C min^{-1}. The latest step was recorded using a thermal conductivity detector.

TEM. Imaging of catalysts was performed in a Philips CM200 transmission electron microscope operating at 200 kV in bright-field mode. Powder samples were deposited over a coated copper grid with lacey carbon before to loading onto the instrument. Histograms of particles sizes included in ESI were done by sampling 180 particles.

XPS. X-ray photoelectron spectroscopy measurements were conducted on a VG-ESCALAB 210 equipment provided of an analysis chamber at ultra-high vacuum conditions (10^{-11} bar) and a SPECS-Phoibos 100 hemispheric analyser. Pelletized samples were loaded to the instrument in a pre-chamber at 10^{-9} bar. The catalysts were excited using an Al Kα x-ray source (1486.6 eV) at 12 kV and 20 mA. Si 2p maximum intensity was set at 103.4 eV for energy calibration, characteristic of silica. High resolution Ni 2p, Ce 3d, O 1s, Si 2p and C 1s spectra were recorded at 50 and 0.1 eV of pass energy and a resolution, respectively. In situ treatments (5% H_2/Ar and CO_2:CH_4 at 750 °C) were carried in a reaction chamber connected to the pre-chamber at atmospheric pressure. The spectra were treated and analysed using CasaXPS v.2.3.17 software.

XAS. X-ray absorption spectroscopy in the EXAFS and XANES regions was recorded at the BM25A beamline of the European Synchrotron Radiation Facility (ESRF), located in Grenoble, France. An optimized amount of catalyst was pelletized and analysed in transmission mode using a cell for in situ gas – solid reactions. XAS spectra were collected at room temperature, 500 and 750 °C in presence of 5% H_2/Ar flow (50 mL min^{-1}) from 8200 to 9100 eV using a step of 0.5 eV. A standard nickel-foil measurement was used for energy calibration. The EXAFS patterns were Fourier transformed in the 1.9–12.5 Å^{-1} range. The treatment and analysis of spectra was carried out using the IFEFFIT software.

Catalytic tests. Reaction tests were conducted in a 4-channel Flowrence XD platform from Avantium. Typically, 10 mg of the catalyst was loaded in a quartz reactor. The catalysts were pelletized to obtain grains sized from 150 to 250 μm before loading. The reactors are 300 mm long quartz tubes inserted in a furnace. The outside and inside diameters of the tubes are 3 and 2 mm, respectively. One reactor was always used without catalyst as a blank. The mixed feed consisted of 1/1/1 ratio of $CH_4/CO_2/N_2$ mixture. We aimed for a WHSV of 60000 mL min^{-1} gcat^{-1}. Prior to feeding the reaction mixture all samples were pre-treated in situ with a pure H_2 atmosphere for 1 hours at 750 °C. Gas product analysis was performed by an Agilent 7890B GC equipped with a TCD detector (H_2, He, CO) and two FID detectors for separate analysis of light hydrocarbons (C1–C9) and oxygenates (CO_2, alcohols). Helium was used as carrier gas for the FID channels. Argon was used as carrier in the TCD channel to enable detection of helium as internal standard and hydrogen as analyte. Conversions (X, %) and carbon balance are defined as follows:

$$\mathrm{Conv_{CO2}}\ (\%) = \frac{\mathrm{CO2_{in}}/\mathrm{He_{in}} - \mathrm{CO2_{out}}/\mathrm{He_{out}}}{\mathrm{CO2_{in}}/\mathrm{He_{in}}} \times 100 \qquad (2)$$

$$Conv_{CH4}\ (\%) = \frac{CH4_{in}/He_{in} - CH4_{out}/He_{out}}{CH4_{in}/He_{in}} \times 100 \quad (3)$$

$$C_{Balance}(\%) = \frac{\sum C_{out}/He_{out}}{\sum C_{in}/He_{in}} \times 100 \quad (4)$$

where Ci_{in} and Ci_{out}, are the concentrations determined by GC analysis in the blank and in the reactor outlet respectively.

Acknowledgements

Funding for this work was provided by "Ministerio de Economia y Competitividad" of Spain (Project Nos. ENE2011-24412 and CTQ2014-60524-R) and King Abdullah University of Science and Technology (KAUST). Alberto Rodriguez-Gomez thanks the Spanish Government for the PhD fellowship (No. BES-2012-061744). We acknowledge ESRF (BM25 SPLINE beamline) for their support. We also thank Sandra Ramirez Cherbuy for artwork and Jullian Vittenet for technical support.

Conflict of Interest

The authors declare no conflict of interest.

Keywords: Dry reforming · Ceria · Coke resistance · in situ XAS · Nickel

[1] E. J. Schelter, *Nat. Chem.* **2013**, *5*, 348–348.
[2] R. J. Gorte, *AIChE J.* **2010**, *56*, 1126–1135.
[3] T. Montini, M. Melchionna, M. Monai, P. Fornasiero, *Chem. Rev.* **2016**, *116*, 5987–6041.
[4] J. Paier, C. Penschke, J. Sauer, *Chem. Rev.* **2013**, *113*, 3949–3985.
[5] J. Papavasiliou, M. Rawski, J. Vakros, G. Avgouropoulos, *ChemCatChem* **2018**, *10*, 2096–2106.
[6] F. B. Noronha, E. C. Fendley, R. R. Soares, W. E. Alvarez, D. E. Resasco, *Chem. Eng. J.* **2001**, *82*, 21–31.
[7] R. B. Duarte, M. Olea, E. Iro, T. Sasaki, K. Itako, J. A. Van Bokhoven, *ChemCatChem* **2014**, *6*, 2898–2903.
[8] V. M. Gonzalez-DelaCruz, J. P. Holgado, R. Pereniguez, A. Caballero, *J. Catal.* **2008**, *257*, 307–314.
[9] A. Bruix, J. A. Rodriguez, P. J. Ramírez, S. D. Senanayake, J. Evans, J. B. Park, D. Stacchiola, P. Liu, J. Hrbek, F. Illas, *J. Am. Chem. Soc.* **2012**, *134*, 8968–8974.
[10] A. Caballero, J. P. Holgado, V. M. Gonzalez-delaCruz, S. E. Habas, T. Herranz, M. Salmeron, *Chem. Commun.* **2010**, *46*, 1097–1099.
[11] X. Du, D. Zhang, L. Shi, R. Gao, J. Zhang, *J. Phys. Chem. Chem. Phys.* **2012**, *116*, 10009–10016.
[12] S. M. Stagg-Williams, F. B. Noronha, G. Fendley, D. E. Resasco, *J. Catal.* **2000**, *194*, 240–249.
[13] S. Damyanova, J. M. C. Bueno, *Appl. Catal. A* **2003**, *253*, 135–150.
[14] M. M. Rahman, T. L. Church, A. I. Minett, A. T. Harris, *ChemSusChem* **2013**, *6*, 1006–1013.
[15] R. B. Duarte, O. V. Safonova, F. Krumeich, M. Makosch, J. A. van Bokhoven, *ACS Catal.* **2013**, *3*, 1956–1964.
[16] N. Wang, K. Shen, L. Huang, X. Yu, W. Qian, W. Chu, *ACS Catal.* **2013**, *3*, 1638–1651.
[17] L. Li, D. H. Anjum, H. Zhu, Y. Saih, P. V. Laveille, L. D'Souza, J. M. Basset, *ChemCatChem* **2015**, *7*,427–433.
[18] Z. Cheng, Q. Wu, J. Li, Q. Zhu, *Catal. Today* **1996**, *30*, 147–155.
[19] S. S. Y. Lin, D. H. Kim, S. Y. Ha, *Appl. Catal. A* **2009**, *355*, 69–77.
[20] S. Y. Foo, C. K. Cheng, T.-H. Nguyen, A. A. Adesina, *Catal. Today* **2011**, *164*, 221–226.
[21] A. Carrero, A. J. Vizcaino, J. A. Calles, L. Garcia-Moreno, *J. Energy Chem.* **2017**, *26*, 42–48.
[22] P. Dutta, S. Pal, M. S. Seehra, Y. Shi, E. M. Eyring, R. D. Ernst, *Chem. Mater.* **2006**, *18*, 5144–5146.
[23] Z. Qiao, Z. Wu, S. Dai, *ChemSusChem* **2013**, *6*, 1821–1833.
[24] V. K. Paidi, L. Savereide, D. J. Childers, J. M. Notestein, C. A. Roberts, J. van Lierop, *ACS Appl. Mater. Interfaces* **2017**, *9*, 30670–30678.
[25] A. Trovarelli, J. Llorca, *ACS Catal.* **2017**, *7*, 4716–4735.
[26] S. Zhang, S. Muratsugu, N. Ishiguro, M. Tada, *ACS Catal.* **2013**, *3*, 1855–1864.
[27] N. Wang, W. Chu, T. Zhang, X. S. Zhao, *Int. J. Hydrogen Energy* **2012**, *37*, 19–30.
[28] N. Wang, Z. Xu, J. Deng, K. Shen, X. Yu, W. Qian, W. Chu, F. Wei, *ChemCatChem* **2014**, *6*, 1470–1480.
[29] C. E. Daza, J. Gallego, F. Mondragón, S. Moreno, R. Molina, *Fuel* **2010**, *89*, 592–603.
[30] I. Luisetto, S. Tuti, C. Battocchio, S. Lo Mastro, A. Sodo, *Appl. Catal. A* **2015**, *500*, 12–22.
[31] V. M. Gonzalez-Delacruz, F. Ternero, R. Pereñíguez, A. Caballero, J. P. Holgado, *Appl. Catal. A* **2010**, *384*, 1–9.
[32] A. Rodriguez-Gomez, R. Pereniguez, A. Caballero, *Catal. Today* **2018**, *307*, 224–230.
[33] A. Rodriguez-Gomez, F. Platero, A. Caballero, G. Colon, *J. Mol. Catal.* **2018**, *445*, 142–151.
[34] X. Ning, Y. Lu, H. Fu, H. Wan, Z. Xu, S. Zheng, *ACS Appl. Mater. Interfaces* **2017**, *9*, 19335–19344.
[35] A. Rodriguez-Gomez, R. Pereniguez, A. Caballero, *J. Phys. Chem. B* **2018**, *122*, 500–510.
[36] M. Akri, S. Zhao, X. Y. Li, K. T. Zang, A. F. Lee, M. A. Isaacs, W. Xi, Y. Gangarajula, J. Luo, Y. J. Ren, Y. T. Cui, L. Li, Y. Su, X. L. Pan, W. Wen, Y. Pan, K. Wilson, L. Li, B. T. Qiao, H. Ishii, Y. F. Liao, A. Q. Wang, X. D. Wang, T. Zhang, *Nat. Commun.* **2019**, *10*, 5181.
[37] E. G. M. Kuijpers, A. K. Breedijk, W. J. J. Van der Wal, J. W. Geus, *J. Catal.* **1983**, *81*, 429–439.
[38] X. Cai, Y. H. Hu, *Energy Sci. Eng.* **2019**, *7*, 4–29.
[39] Y. H. Hu, E. Ruckenstein, in *Advances in Catalysis* (Eds.: B. C. Gates, H. Knozinger), Elsevier Academic Press Inc, San Diego, **2004**, pp 297–345.
[40] Y. H. Hu, E. Ruckenstein, *Appl. Catal. A* **1995**, *133*, 149–161.
[41] Y. H. Hu, E. Ruckenstein, *Catal. Rev. Sci. Eng.* **2020**, *44*, 423–453.
[42] R. Pereñiguez, V. M. Gonzalez-delaCruz, A. Caballero, J. P. Holgado, *Appl. Catal. B* **2012**, *123–124*, 324–332.
[43] R. Pereñiguez, V. M. Gonzalez-delaCruz, J. P. Holgado, A. Caballero, *Appl. Catal. B* **2010**, *93*, 346–353.
[44] S. Das, J. Ashok, Z. Bian, N. Dewangan, M. H. Wai, Y. Du, A. Borgna, K. Hidajat, S. Kawi, *Appl. Catal. B* **2018**, *230*, 220–236.
[45] Ş. Özkara-Aydınoğlu, E. Özensoy, A. E. Aksoylu, *Int. J. Hydrogen Energy* **2009**, *34*, 9711–9722.
[46] Z. Alipour, M. Rezaei, F. Meshkani, *J. Ind. Eng. Chem.* **2014**, *20*, 2858–2863.
[47] K. S. W. Sing, D. H. Everett, R. A. W. Haul, L. Moscou, R. A. Pierotti, J. Rouquerol, T. Siemieniewska, *Pure Appl. Chem.* **1985**, *57*, 603–619.
[48] A. Rodriguez-Gomez, A. Caballero, *ChemNanoMat* **2017**, *3*, 94–97.
[49] J.-Y. Luo, M. Meng, J.-S. Yao, X.-G. Li, Y.-Q. Zha, X. Wang, T.-Y. Zhang, *Appl. Catal. B* **2009**, *87*, 92–103.
[50] E. Gaigneaux, M. Devillers, S. Hermans, P. A. Jacobs, J. Martens, P. Ruiz, *Scientific Bases for the Preparation of Heterogeneous Catalysts: Proceedings of the 10th International Symposium*, July 11–15, Elsevier, Louvain-la-Neuve, Belgium, **2010**.
[51] C. Xu, Y. Wu, S. Li, J. Zhou, J. Chen, M. Jiang, H. Zhao, G. Qin, *J. Mater. Sci. Technol.* **2020**, *40*, 39–46.
[52] M. A. A. Aziz, A. A. Jalil, S. Wongsakulphasatch, D. N. Vo, *Catal. Sci. Technol.* **2020**, *10*, 35–45.
[53] P. Burroughs, A. Hamnett, A. F. Orchard, G. Thornton, *J. Chem. Soc. Dalton Trans.* **1976**, 1686–1698.
[54] E. Bêche, P. Charvin, D. Perarnau, S. Abanades, G. Flamant, *Surf. Interface Anal.* **2008**, *40*, 264–267.
[55] S. Deshpande, S. Patil, S. Kuchibhatla, S. Seal, *Appl. Phys. Lett.* **2005**, *87*, 133113.
[56] D. R. Mullins, S. H. Overbury, D. R. Huntley, *Surf. Sci.* **1998**, *409*, 307–319.
[57] F. Zhang, P. Wang, J. Koberstein, S. Khalid, S.-W. Chan, *Surf. Sci.* **2004**, *563*, 74–82.

[58] M. V. Ganduglia-Pirovano in *Defects at Oxide Surfaces* (Eds.: J. Jupille, G. Thornton), Springer International Publishing, Cham, **2015**, pp 149–190.
[59] V. Calvino-Casilda, A. J. López-Peinado, R. M. Martín-Aranda, E. P. Mayoral in *Nanocatalysis: Applications and Technologies*, CRC Press, **2019**.
[60] K. O. Hodgson, B. Hedman, J. E. Penner-Hahn in *EXAFS and Near Edge Structure III: Proceedings of an International Conference, July 16–20*, Springer Berlin Heidelberg, Stanford, CA, **1984**.
[61] A. Anspoks, A. Kalinko, R. Kalendarev, A. Kuzmin, *Phys. Rev. B* **2012**, *86*, 174114.
[62] J. De Graaf, A. J. Van Dillen, K. P. De Jong, D. C. Koningsberger, *J. Catal.* **2001**, *203*, 307–321.
[63] A. Jentys, *Phys. Chem. Chem. Phys.* **1999**, *1*, 4059–4063.
[64] J. Matos, L. K. Ono, F. Behafarid, J. R. Croy, S. Mostafa, A. T. DeLaRiva, A. K. Datye, A. I. Frenkel, B. Roldan Cuenya, *Phys. Chem. Chem. Phys.* **2012**, *14*, 11457–11467.
[65] D. Pakhare, J. Spivey, *Chem. Soc. Rev.* **2014**, *43*, 7813–7837.
[66] J. Zhang, H. Wang, A. K. Dalai, *J. Catal.* **2007**, *249*, 300–310.
[67] J.-H. Kim, D. J. Suh, T.-J. Park, K.-L. Kim, *Appl. Catal. A* **2000**, *197*, 191–200.
[68] S. Tang, L. Ji, J. Lin, H. C. Zeng, K. L. Tan, K. Li, *J. Catal.* **2000**, *194*, 424–430.
[69] Y. Song, E. Ozdemir, S. Ramesh, A. Adishev, S. Subramanian, A. Harale, M. Albuali, B. A. Fadhel, A. Jamal, D. Moon, S. H. Choi, C. T. Yavuz, *Science* **2020**, *367*, 777–++.
[70] C. Montero, A. Ochoa, P. Castano, J. Bilbao, A. G. Gayubo, *J. Catal.* **2015**, *331*, 181–192.
[71] Z. Wang, X. M. Cao, J. Zhu, P. Hu, *J. Catal.* **2014**, *311*, 469–480.
[72] J. C. Guevara, J. A. Wang, L. F. Chen, M. A. Valenzuela, P. Salas, A. García-Ruiz, J. A. Toledo, M. A. Cortes-Jácome, C. Angeles-Chavez, O. Novaro, *Int. J. Hydrogen Energy* **2010**, *35*, 3509–3521.
[73] D. Zhao, J. Feng, Q. Huo, N. Melosh, G. H. Fredrickson, B. F. Chmelka, G. D. Stucky, *Science* **1998**, *279*, 548–552.
[74] E. P. Barrett, L. G. Joyner, P. P. Halenda, *J. Am. Chem. Soc.* **1951**, *73*, 373–380.
[75] S. Brunauer, P. H. Emmett, E. Teller, *J. Am. Chem. Soc.* **1938**, *60*, 309–319.
[76] P. Malet, A. Caballero, *J. Chem. Soc. Faraday Trans. 1* **1988**, *84*, 2369–2375.

Manuscript received: September 20, 2020
Revised manuscript received: October 17, 2020
Accepted manuscript online: October 29, 2020
Version of record online: November 19, 2020